

# Sub-1-Volt Electrically Programmable Optical Modulator Based on Active Tamm Plasmon

Joo Hwan Ko, Dong Hyun Seo, Hyeon-Ho Jeong, Sejeong Kim,\* and Young Min Song\*

Reconfigurable optical devices hold great promise for advancing high-density optical interconnects, photonic switching, and memory applications. While many optical modulators based on active materials have been demonstrated, it is challenging to achieve a high modulation depth with a low operation voltage in the near-infrared (NIR) range, which is a highly sought-after wavelength window for free-space communication and imaging applications. Here, electrically switchable Tamm plasmon coupled with poly(3,4-ethylenedioxythiophene):polystyrene sulfonate (PEDOT:PSS) is introduced. The device allows for a high modulation depth across the entire NIR range by fully absorbing incident light even under epsilon near zero conditions. Optical modulation exceeding 88% is achieved using a CMOS-compatible voltage of  $\pm 1$  V. This modulation is facilitated by precise electrical control of the charge carrier density through an electrochemical doping/dedoping process. Additionally, the potential applications of the device are extended for a non-volatile multi-memory state optical device, capable of rewritable optical memory storage and exhibiting long-term potentiation/depression properties with neuromorphic behavior.

Conventionally, optical modulation has been achieved using the electro-optic effect, which changes the refractive index in response to an applied electric field; however, the electro-optic coefficients observed in native materials are typically small.<sup>[5,6]</sup> Alternatively, a particularly promising avenue lies in utilizing active materials that can modulate carrier densities, allowing for the direct manipulation of plasmonic effects and transforming material optical constants.<sup>[7–9,10]</sup> To this point, a wide range of materials have been thoroughly investigated as viable candidates for active materials; however, the challenge of fulfilling various requirements to create an efficient reconfigurable component still remains.<sup>[11–13]</sup> Several key criteria include compact physical size, easy device fabrication, and a high modulation depth, preferably with low operation voltage.<sup>[1,14–16]</sup> Additionally, a non-volatile nature is preferred due to its ability to decrease energy consumption resulting from its pulsed

## 1. Introduction

Reconfigurable optical modulators play a pivotal role in building various components in integrated photonics, such as optical interconnects, photonic switches, and optical memories.<sup>[1–4]</sup>

operation.<sup>[17–19]</sup> An electrical switching capability is also favorable as it would facilitate the simultaneous control of multiple optical modulators at the device level.

However, achieving complete on-off optical modulation remains a challenge in any material system, and this task becomes increasingly difficult in the near-infrared (NIR) region.<sup>[3]</sup> The complexity arises because the plasma frequency ( $\omega_p$ ) for typical active materials is higher than NIR, resulting in ineffective modulation due to a diminutive absorption coefficient.<sup>[8,10,17,20,21]</sup> Therefore, many optical modulators have only achieved a high modulation depth at mid-IR or longer range.<sup>[2,9,22–24]</sup> In order to address this issue, it is important to thoroughly select both the active material and the device geometry, as both aspects impact the performance of the modulator.

Among many promising active materials, the material of the focus in this study is a poly(3,4-ethylenedioxythiophene):polystyrene sulfonate (PEDOT:PSS), a tunable conductive polymer. The PEDOT:PSS can efficiently switch between metallic and insulating states through applied voltages of less than 1 V. Furthermore, its non-volatile state and the presence of bistability collectively open up a multitude of opportunities for its use in photonic devices.<sup>[15,25]</sup> Despite its potential as an active material, standalone PEDOT:PSS lacks the level of light-matter interaction required to attain full on-off operation. These challenges have been addressed through various approaches,

J. H. Ko, D. H. Seo, H.-H. Jeong, Y. M. Song  
 School of Electrical Engineering and Computer Science  
 Gwangju Institute of Science and Technology  
 Gwangju 61005, Republic of Korea  
 E-mail: [ymsong@gist.ac.kr](mailto:ymsong@gist.ac.kr)

H.-H. Jeong, Y. M. Song  
 Department of Semiconductor Engineering  
 Gwangju Institute of Science AND Technology  
 Gwangju 61005, Republic of Korea

S. Kim  
 Department of Electrical and Electronic Engineering  
 University of Melbourne  
 Victoria 3000, Australia  
 E-mail: [sejeong.kim@unimelb.edu.au](mailto:sejeong.kim@unimelb.edu.au)

Y. M. Song  
 AI Graduate School  
 Gwangju Institute of Science and Technology  
 Gwangju 61005, Republic of Korea

 The ORCID identification number(s) for the author(s) of this article can be found under <https://doi.org/10.1002/adma.202310556>

DOI: 10.1002/adma.202310556

such as plasmonic resonators or Mie resonators, both derived from nanoantennas and coupling states. Nevertheless, even with these structures, the suboptimal metallic property (low extinction coefficient) of PEDOT:PSS in the NIR not only results in inadequate light-matter interaction but also entails complex and costly manufacturing processes. As an alternative, Tamm plasmons have recently emerged as fascinating platforms, harnessing their subtle metallic properties to efficiently absorb light through the precise matching of conjugate impedance, even with non-sophisticated planar structures.<sup>[26,27]</sup>

Here, we report a near-unity optical modulation using electrically controllable Tamm plasmon (ECTP) coupled with PEDOT:PSS. Tamm plasmon mode appears when the optical structure consists of a planar metal and a distributed Bragg reflector (DBR).<sup>[26,27]</sup> The optical mode is concentrated at the metal-DBR interface; thus, the insertion of an active layer at the interface allows incident light to effectively respond to any change in the active material. PEDOT:PSS possesses optical characteristics that facilitate efficient and rapid conversion between a lossless state (i.e., dielectric) and an absorption state (i.e., metallic), with a  $\omega_p$  in the high frequency of 1300 nm. Through the utilization of advantages from the Tamm plasmon-coupled active material, we achieved an experimental modulation depth of 88%, while the theoretical value projects this value to surpass 99%. To the best of the authors' knowledge, this is the highest modulation depth achieved at a frequency higher than the plasma frequency. Our device also maintains a high modulation depth across a broad spectrum range spanning from 800 to 2500 nm. This remarkable modulation depth is attributed to the combination effect from both the design, which involves an impedance-matched Tamm plasmon cavity, and the material, which possesses a non-negligible extinction coefficient ( $k$ ) value. The device presents a high modulation depth at  $\omega > \omega_p$ , only using sub-1-volt input voltage, compatible with the conventional CMOS voltage standard of 3.3 V.<sup>[15]</sup> Finally, this work extends to the practical demonstration of PEDOT:PSS-based devices: an optical memory and an optical neuromorphic device. The hysteresis curve in response to the applied cyclic voltage is measured. An array of modulator cells that are electrically programmable and optically readable memory is demonstrated. Finally, the photonic neuromorphic system showing optical long-term potentiation (LTP) and long-term depression (LTD) is experimentally verified. This work paves the path for the advancement of reconfigurable optical components.

## 2. Results and Discussion

### 2.1. ECTP with High Modulation Depth

The schematic illustration in **Figure 1a** shows the ECTP array with counter electrodes (CE) and working electrodes (WE). Each ECTP cell has the ability to control the reflectivity from nearly zero to one by adjusting the applied voltage from +1 V to -1 V (**Figure 1a**, inset). **Figure 1b** shows the chemical structures of PEDOT:PSS in its insulating and metallic states. The potential of the polymer causes doping (+1 V) and de-doping (-1 V), effectively regulating the carrier density to reach  $\approx 6.5 \times 10^{20} \text{ cm}^{-3}$  in the metallic state.<sup>[15]</sup> **Figure 1c** describes the detailed Tamm plasmon structure consisting of three layered parts, i.e., i) DBR on ii) PEDOT:PSS active layer and iii) Au membrane. As depicted in

**Figure 1c**, the strong electric field is confined at the interface between DBR and PEDOT:PSS when PEDOT:PSS is in the metallic state, resulting in strong light absorption and narrow linewidth in the spectrum. In the insulating state, the electric field extends beyond the PEDOT:PSS layer, causing the incident light to be reflected by the Au layer. This distinctive response results in a high level of modulation in reflectance, surpassing 99% in numerical simulation (**Figure 1d**).

The modulation depth achieved in this work is compared to the values from previous works and displayed in **Figure 1e**. The ECTP structure demonstrates higher modulation depths compared to other optical reconfigurable photonics systems reliant on tunable materials, such as conducting oxides (e.g., indium tin oxide (ITO)<sup>[8,9,10]</sup> and indium silicon oxide (ISO)<sup>[28]</sup>), graphene,<sup>[22,29–32]</sup> and phase change materials (e.g., germanium antimony tellurium (GST),<sup>[33–36]</sup>  $\text{VO}_2$ <sup>[2,20,21,37]</sup>). While numerous tunable devices comprising active materials integrated with nanophotonic structures have demonstrated modulation capabilities,<sup>[20,28,35,38,8]</sup> the inherent limitations impede the achievement of complete modulation efficacy. Some fundamental drawbacks include that the charge accumulation (or depletion) layer of conducting oxides is extremely thin, implicitly indicating the weakness of field-matter interaction.<sup>[39,7]</sup> Graphene-based modulators have achieved significant modulation depth; however, their plasma frequencies ( $\omega_p$ ) fall within the IR–THz range, making them unsuitable for optical modulators in the NIR range.<sup>[40]</sup> In this work, the modulation depth theoretically exhibits 99% across the NIR range ( $\lambda_{\text{res}} = 800\text{--}2500 \text{ nm}$ ), while the experimental result shows 88% and 80% at  $\lambda_{\text{res}} = 1500$  and 970 nm, respectively (**Figures S7** and **S8**, Supporting Information). We acknowledge that we presented the measured modulation depth as maximum values. At this point, slight variations from uniformity issues occurred during the spin-coating process, and these will be discussed in the structural analysis section (**Figure 3f**). The enhanced modulation depth can primarily be attributed to three factors. First, the robust light confinement facilitated by the Tamm plasmon allows for strong light absorption, even with the suboptimal metallic property (i.e.,  $\epsilon_r \approx 0$ ) of PEDOT:PSS. Second, the lossless state (real part of the dielectric function,  $\epsilon_r > 1$ ) of PEDOT:PSS ensures maximum light reflection. Third, the higher  $\omega_p$  (1300 nm) of PEDOT:PSS compared to other active materials (**Table S1**, Supporting Information) allows the device operation in the shorter NIR range. Notably, only this work achieves a high modulation depth of over 50% under the conditions where  $\epsilon_r$  is positive, and the target resonance frequency is over  $\omega_p$ . In addition, low operational power is vital for compatibility with standard CMOS operations (<3.3 V). In this regard, **Figure 1f** shows that PEDOT:PSS stands out with its small operating voltage ( $\pm 1 \text{ V}$ ). Furthermore, on the  $x$ -axis, the  $\omega_p$  of each material is depicted. Among them, the  $\omega_p$  of PEDOT:PSS is distinguished by having the highest value, enabling its applicability to the short wavelength range around the NIR region.

### 2.2. Computational Modeling of Active Tamm Plasmon

**Figure 2a** shows a structure illustration used for the computational modeling of active Tamm plasmon (**Note 1** and

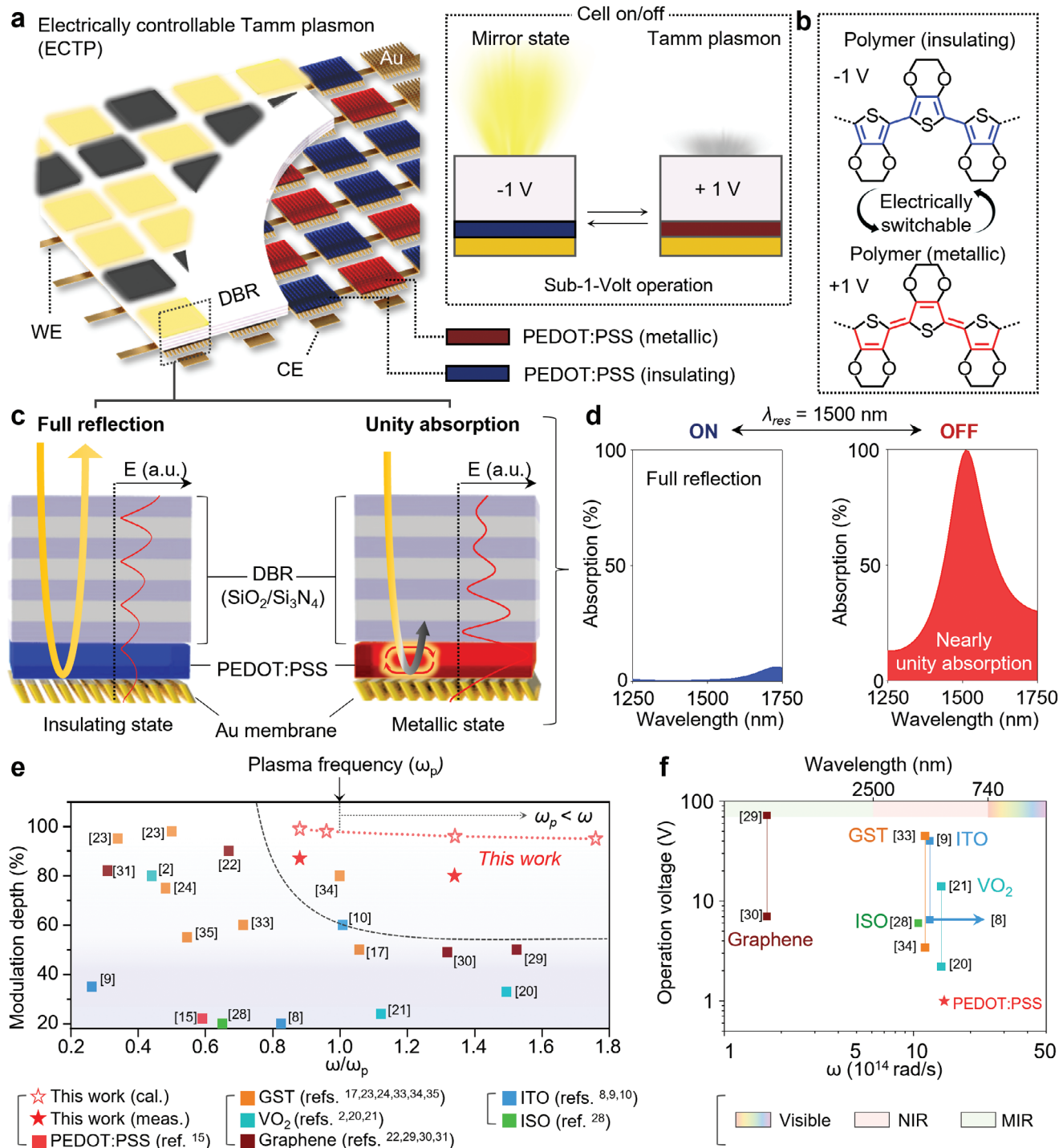


**Figure 1.** Electrically controllable Tamm plasmon (ECTP) resonator with high on/off modulation ratio. **a**) Schematic illustration of the ECTP array. From the top to the bottom, each cell consists of a distributed Bragg reflector (DBR), poly(3,4-ethylenedioxythiophene):poly(styrene sulfonate) (PEDOT:PSS), and Au membrane. Each ECTP cell is controlled by a working electrode (WE) and a counter electrode (CE). The inset shows on/off operation by alternating between the mirror and Tamm plasmon states using a sub  $\pm 1$  V operational voltage. **b**) The molecular configuration of PEDOT:PSS and its electrically switchable optical state, alternating between insulating and metallic states. **c**) Schematic cross-sectional illustrations with structural details and the electric field profile when the cell operates as a reflector and an absorber, respectively. In the Tamm state, the electric field is strongly confined to the PEDOT:PSS layer. **d**) Simulated absorption spectra at the target wavelength, 1500 nm, where the ECTP exhibits full reflection (ON, insulating state) and nearly unity absorption (OFF, metallic state), respectively. **e**) Comparison of the modulation depth of various actively tunable photonic devices. The operating frequency ( $\omega$ ) is divided by each active material's plasma frequency ( $\omega_p$ ). **f**) The operational voltages for active materials utilized in the reference papers in (e) and their working wavelength range.

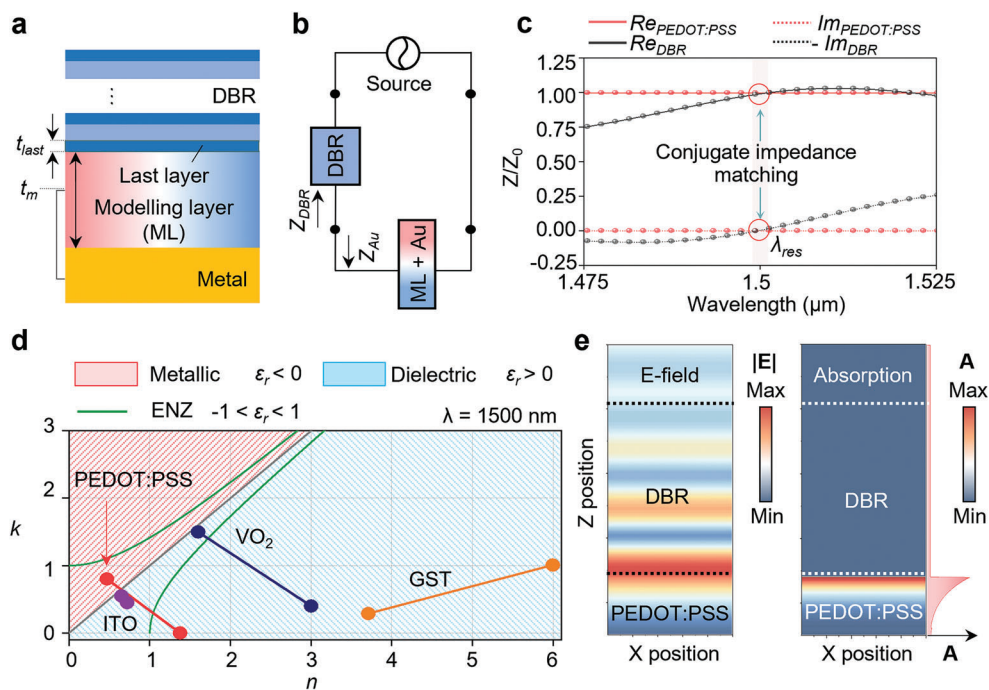


**Figure 2.** Structural analysis of ECTP with optical switching mechanism. a) A schematic depicting the Tamm plasmon resonator used in optical calculation. b) Equivalent conjugate-matching circuit. c) Optical impedances ( $Z/Z_0$ ) as functions of wavelength (Re and Im indicate real and imaginary components, respectively). d) Complex refractive index of active materials. e) Simulated electric field (left) and absorption profile (right) using the PEDOT:PSS in its metallic state.

Figures S1–S5, Supporting Information). The DBR is stacked with three pairs of  $\text{SiO}_2/\text{Si}_3\text{N}_4$  on the last layer ( $\text{Si}_3\text{N}_4$ ). For the Tamm plasmon state, the resonant wavelength ( $\lambda_{\text{res}}$ ) should be placed at the center wavelength of the stop band driven by DBR. The thickness of the DBR layer can be obtained by calculating the quarter wavelength in the medium, for example,  $t = \lambda_{\text{res}}/4n$ , where  $n$  is an effective refractive index of the DBR. The equation yields thickness values of 259 and 188 nm for  $\text{SiO}_2$  and  $\text{Si}_3\text{N}_4$  at a resonance wavelength ( $\lambda_{\text{res}}$ ) of 1500 nm. Subsequently, the thickness of the last layer ( $t_{\text{last}}$ ), 83 nm, was obtained from the following relation:<sup>[41]</sup>  $1 - r_{\text{PEDOT:PSS}} r_{\text{DBR}} \exp(2ikn_{\text{last}}t_{\text{last}}) \approx 0$ , where  $r_{\text{PEDOT:PSS}}$  is the reflection coefficient of a wave incident on the PEDOT:PSS and  $r_{\text{DBR}}$  is the reflection coefficient of a wave incident on the DBR from  $\text{Si}_3\text{N}_4$  last layer. Next, we optimized the impedance by using an equivalent conjugate-matching circuit to achieve narrowband and unity absorption. Conjugate impedance matching is a standard method in transmission line theory that aims to optimize power transfer from the source to the load, leading to a relation expressed as  $Z_{\text{PEDOT:PSS}} = Z_{\text{DBR}}^*$ , where  $Z_{\text{PEDOT:PSS}}$  is the impedance of the PEDOT:PSS layer, and  $Z_{\text{DBR}}^*$  is the conjugate impedance of the DBR surface. The equivalent circuit diagram of Figure 2a is illustrated in Figure 2b for the conjugate-matched transmission line model of the ECTP structure. By considering metallic PEDOT:PSS as a modeling layer, we calculated  $Z_{\text{PEDOT:PSS}}$  and  $Z_{\text{DBR}}^*$ . Figure 2c shows numerically calculated real and imaginary parts of optical impedances, where  $Z_0 = \sqrt{\mu_0/\epsilon_0}$  is the vacuum impedance and  $\mu_0$  and  $\epsilon_0$  represent the vacuum permeability and permittivity, respectively. The imaginary part of the optical impedance has opposite values between DBR and PEDOT:PSS, while the real parts have the same values at 1500 nm.

This leads to an optical Tamm state at the interface between DBR and PEDOT:PSS, enabling near-perfect absorption. In these conditions, the Tamm state's presence is ensured because the optical impedance of a surface is directly tied to the material's topological properties in the bulk, mediated by the geometric phases (i.e., Zak phase) in its photonic bands.<sup>[42]</sup>

The range of possible changes in refractive index for various active materials including PEDOT:PSS, GST, ITO, and  $\text{VO}_2$  is displayed in a complex refractive index diagram as shown in Figure 2d. Based on the  $\epsilon_r$  value ( $\epsilon_r = n^2 - k^2$ ), the domain is classified into three sectors: metallic ( $\epsilon_r < 0$ ), dielectric ( $\epsilon_r > 0$ ), and epsilon near zero where  $\epsilon_r$  is between  $-1$  and  $1$ . Notably, only PEDOT:PSS exhibits varying optical properties across both the metallic and dielectric regions, leading to efficient on/off modulation of Tamm plasmons. In contrast, ITO,  $\text{VO}_2$ , and GST exclusively vary their optical properties within the dielectric domain, resulting in a small modulation depth. Figure S9, Supporting Information shows numerically simulated absorption spectra, demonstrating the theoretically attainable maximum on/off ratio, when the active layer of the device is replaced with PEDOT:PSS,  $\text{VO}_2$ , GST, and ITO. Materials apart from PEDOT:PSS show reduced modulation depth, and ITO has an inherent drawback due to its extremely thin ( $< 2$  nm) charge accumulation layer, hindering efficient absorption in the Tamm state.<sup>[7]</sup> Figure 2e depicts the simulated electric-field magnitude profiles and absorption at the resonance wavelength. The electric field profile shows a distinct standing-wave pattern, with the highest intensity appearing at the interface between the DBR and the PEDOT:PSS (a metallic state) layer. It is important to note that Tamm plasmon fully absorbs the confined electric field placed at the interface of

a metallic layer, even in weak metallic property of PEDOT:PSS in NIR wavelength range. The electric field and absorption profile in the insulating state are presented in Figure S10, Supporting Information. Also, the characteristics of the Tamm plasmon mode are influenced by adjustments to the DBR layer configuration, specifically the material combination (refractive index contrast of DBR) and the number of DBR pairs. These modifications not only impact the sharpness of the Tamm plasmon mode but also its angular dependency (Figures S11 and S12, Supporting Information).<sup>[26]</sup>

### 2.3. Structural Analysis of ECTP with an Optical Switching Mechanism

Figure 3a illustrates the schematic of an ECTP unit cell with charge carriers. The blue and orange circles represent counterions and electrons, respectively. The arrows in the figure indicate the exchange of charge carriers during the doping and dedoping process. The PEDOT:PSS layer absorbs and releases counterions to maintain charge balance corresponding to the electron transfer associated with the positive and negative voltage, respectively. Figure 3b shows that the porous Au layer facilitates the movement of counterions between the electrolyte and the PEDOT:PSS layer, whereas the dense Au layer blocks the counterion exchange. The porous Au layer, deposited by the glancing angle deposition (GLAD), exhibits minimal degradation of electrical properties (three times degraded), and its surface roughness is merely 2–4 nm compared to the dense Au layer.<sup>[43,44]</sup> As a proof of concept, we measured current against applied voltage (versus Ag/AgCl) for different metal structures (dense and porous Au). Figure 3c shows the cyclic-voltammetry plot of the ECTP with a porous layer (red line) and without it (blue line). The ECTP incorporating a porous Au layer exhibits a peak current 13 times higher than the one without it. This significant increase in peak current indicates the fast ion exchanges through Au nanocolumns. We have also experimentally verified that the porous Au layer maintains a high level of reflectance similar to that of a dense Au layer, indicating that the porosity does not degrade the quality of the Tamm state (Figure S13, Supporting Information). Furthermore, the ECTP with porous Au exhibited a notable increase in switching time, recording 339 and 237 ms during dedoping and doping processes, respectively, as opposed to the Tamm plasmon with dense Au (Figure S14, Supporting Information). However, the switching time of the ECTP appears relatively sluggish when compared to the PEDOT:PSS-based metasurface, primarily due to constrained ion exchange. In our pursuit of enhancing the modulation speed for ECTPs, we propose the removal of the Au reflector and the insertion of a conducting layer with ITO between the PEDOT:PSS and DBR layers. This modification results in an improved response time, measured at 221 and 181 ms, while maintaining a 70% modulation depth (Figures S14 and S15, Supporting Information). Additionally, recent studies have reported improvements in the switching speed of electrochemical devices based on PEDOT:PSS by introducing an ion membrane into the polymer channel. This approach reduces the moving distance of ions participating in electrochemical reactions, thus enhancing the doping/dedoping speed.<sup>[45]</sup> Building on these efforts, it is antici-

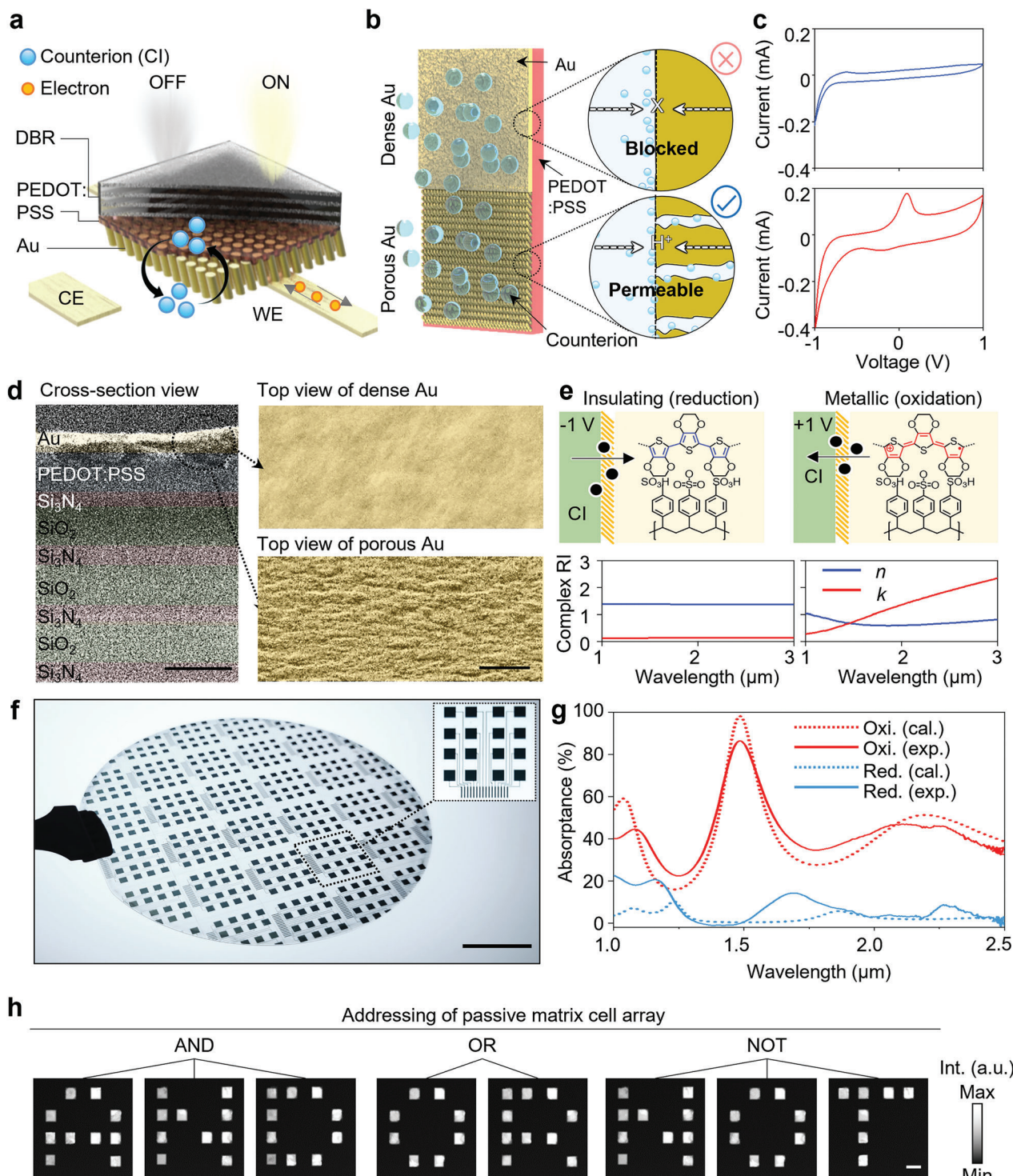
pated that further improvements in modulation speed can be achieved.

Figure 3d is a cross-sectional scanning electron microscopy (SEM) image demonstrating alternating layers in the ECTP unit cell. The top view SEM images show a smooth surface for dense Au (upper right) and a textured surface for porous Au (bottom right). Due to the enhanced permeability of the counterion in ECTP with porous Au, the redox process is promoted due to the fast exchange of counter ions, resulting in complete modulation of complex refractive index (Figure 3e). When the oxidation reaction occurs, the  $k$  value is significant, indicating the material exhibits metallic behavior, while the reduction reaction results in a material with nearly zero, revealing its dielectric properties. In the metallic state, the  $k$  value tends to decrease as the wavelength gets shorter, implying the difficulty of achieving an efficient light modulator in the shorter wavelength range.

A 4-inch wafer-scale ECTP array is fabricated based on the process advantage that each layer can be constructed using scalable fabrication methods, as shown in Figure 3f (see Methods). We note that PEDOT:PSS offers a flexible and customizable scaling factor (Figure S16, Supporting Information). Also, the previous works provided substantial support for the potential scaling down of our structure to the tens of nanometer scale.<sup>[15,46]</sup> Figure 3g displays experimentally obtained absorption spectra (solid lines) from a single ECTP cell. These results closely match with the numerically predicted curves (dotted lines) in terms of both line shape and peak values. The ECTP cell is used to showcase individually addressable ECTP cells, forming letters “AND,” “OR,” and “NOT” as shown in Figure 3h. A detailed explanation of passive matrix addressing is provided in Figure S17, Supporting Information. Each pixel demonstrates a consistently similar reflected intensity, with subtle divergences both between pixels and within an individual pixel (see Figure S18, Supporting Information). These discrepancies arise from the inherent non-uniformity associated with the spin coating method.<sup>[47]</sup> While this method yields an overall uniform coating, its inherent non-uniformity may present challenges in precision applications or during scalable fabrication. To address this concern, recent developments in coating techniques for PEDOT:PSS have been introduced, especially those utilizing electrodeposition methods. Of particular note among these techniques are potentiodynamic deposition and galvanostatic deposition, both showing potential in improving the observed low roughness in the PEDOT:PSS film.<sup>[48]</sup> We believe that these approaches could improve the uniformity issues.

### 2.4. Electrically Triggered Optical Response and Programmable Memory Functions

The suggested optical modulator has the potential for use in optical memory applications owing to the optical hysteresis reported from PEDOT:PSS. Figure 4a depicts an illustrative picture outlining the concept of programmable ECTP, whereby electrical pulses with positive and negative potentials are used to define the information state within the cell. The inset of Figure 4a illustrates the circuitry modeling of the photonic cell with electrical parts (electrode and its relations). Figure 4b shows the reflectance data points obtained during an increasing voltage sweep from  $-1$  V



**Figure 3.** Characterization of proton-based electrochemical reaction with Au membrane. a) Illustration of the unit cell of the ECTP. The porous Au membrane facilitates counterion transport. b) Schematic of permeability of counterion over dense and porous Au film. c) Cyclic-voltammetry (CV) curve of the ECTP with porous Au membrane (red line) and dense Au film (blue line) with a reference electrode (Ag/AgCl). d) Cross-sectional view of scanning electron microscope (SEM) image (left) and top view SEM image (right) of ECTP with dense Au electrode and porous Au membrane. Scale bar is 500 nm. e) Schematic of transport of counterion and electrochemical redox reaction under the applied voltage (top), and corresponding complex refractive index change of PEDOT:PSS (bottom). f) Photo image of wafer-scale (4-inch) ECTP array. The inset shows an individual cell. The scale bar is 2 cm. g) Measured and simulated absorbance spectra of ECTP under oxidized state (red line) and reduced state (blue line), respectively. h) Short-wavelength infrared (SWIR) image of the passive-matrix-based individual cell with on/off function, which represents letters of “AND” (left), “OR” (middle), and “NOT” (right). The scale bar is 3 mm.

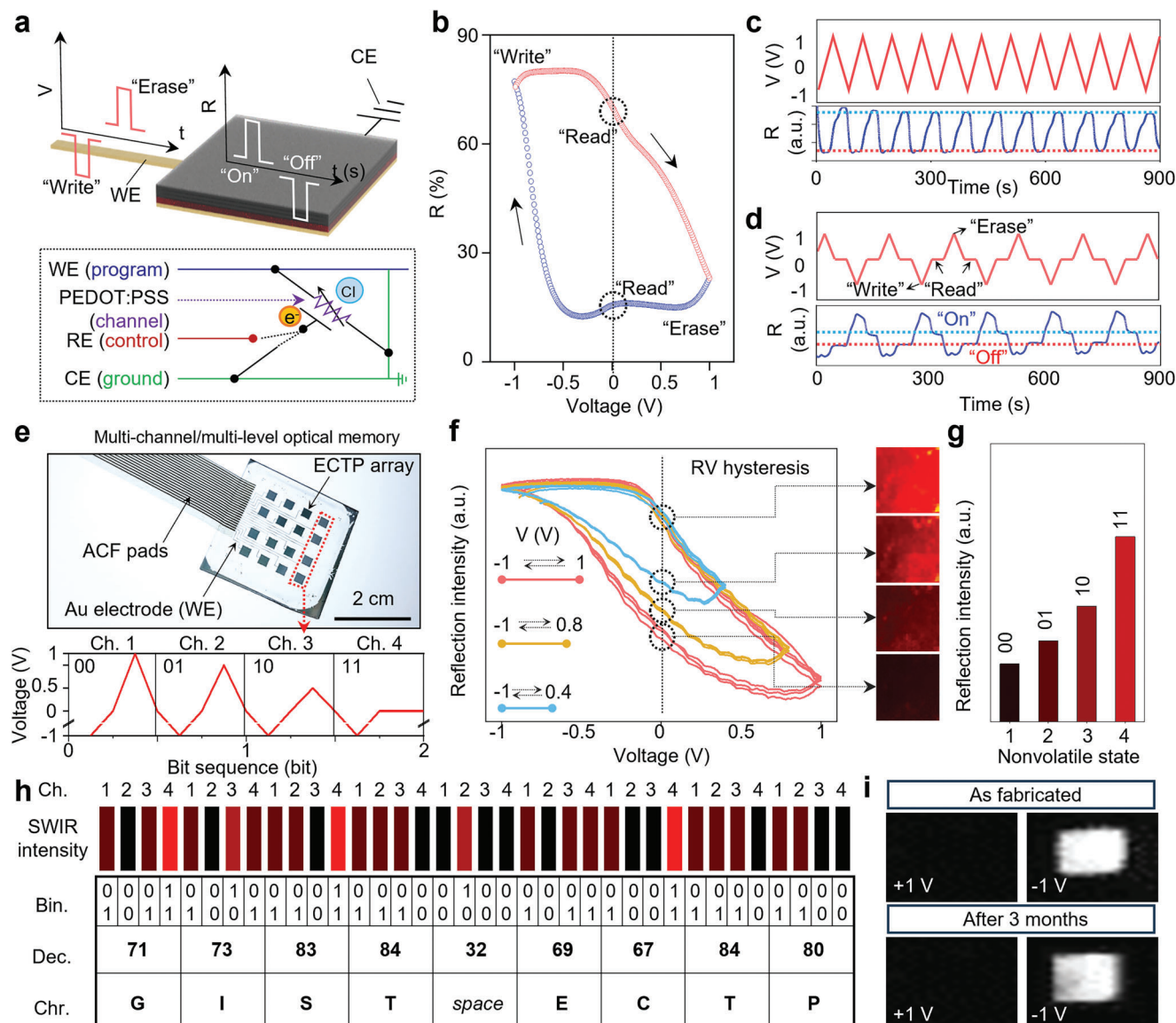


**Figure 4.** Electrically triggered optical response and programmable memory functions. a) Schematic illustration of an electrically programmable and optically readable memory cell (top). Circuitry modeling of the memory cell based on electrochemically active polymer (bottom). b) Hysteresis curve of reflectance–voltage (RV) with the memory operation (write, read, and erase). c) Variation of reflectance in response to cyclical input voltage. d) Memory functions as optical logic under multiple cycles of write, read, and erase. e) Photo image of ECTP with pixelated cells (top). Sweep range of applied voltage on each cell for the multi-bit memory function (bottom). f) RV hysteresis with different sweep ranges with four multi-memory states (left). SWIR reflection image of four states (right). g) Measured reflectance of (f) and corresponding bit level (e.g., 00, 01, 10, and 11). h) Encoded pixel intensity with binary/ASCII code and decoding result. The abbreviations of “Ch.,” “Bin.,” “Dec.,” and “Chr.” represent channel, binary, decimal, and character, respectively. i) SWIR images with intensity tuning of ECTP under the NIR illumination before and after 3 months.

to 1 V followed by a decreasing voltage sweep, revealing a hysteresis loop, that is, reflectance–voltage (RV) hysteresis.<sup>[15,2]</sup> Notably, two clearly distinguishable reflectance values are obtained at 0 V, exhibiting a non-volatile substantial intensity difference with  $\approx 60\%$  switching contrast (Figure 4b). These inherent properties can be effectively employed and converted into digital signals, providing advantages in the fields of data storage and communication. Figure 4c demonstrates a modulation of reflectance using a series of triangular input voltage signals. To demonstrate non-volatile switching between on and off states, we utilized a

negative (−1 V) pulse for the “Write” operation, a positive (1 V) pulse for the “Erase” operation, and paused at 0 V for the “Read” phase in between. As shown in Figure 4d, the process clearly demonstrated an electrically programmable and erasable read-only memory effect.

The large contrast observed in the “Read” phase values allows for the implementation of multi-level memory by utilizing various maximum voltage values. For multi-channel, multi-level demonstration, we constructed a  $4 \times 4$  ECTP cell array and attached them to the control board with an anisotropic

conductive film pad for controlling the electric potential of each cell (Figure 4e, top), where each channel deploys a different programmed electrical potential, thereby demonstrating four states that collectively represents a 2-bit sequence (Figure 4e, bottom). RV hysteresis loops with three different voltage sweep ranges are shown in Figure 4f, demonstrating the four different reading values at 0 V. The operation of a multi-level memory enhances the memory capacity achievable within a single chip. At each reflectance reading at 0 V, the short-wave infrared (SWIR) camera captured images with distinctly varying reflection intensities. Figure 4g shows the acquired reflection intensity, which corresponds to a 2-bit state represented by the binary combinations 00, 01, 10, and 11.

Finally, the ECTP array is used to encode and decode the American Standard Code for Information Interchange (ASCII) code. We encoded the letters “GIST ECTP” in ASCII code by applying different voltage sweep ranges and then decoded the same letter by reading the reflectance (Figure 4h). The specific voltage sweep range used for the encoding process is provided in Figure S19, Supporting Information. We note that our pixels have reliably operated for over 3 months (Figure 4i); however, as shown in the SWIR images, there appears to be a slight degradation. Possible factors contributing to this may include the volume expansion of the polymer during switching and irreversible reactions during electrochemical oxidation and reduction.<sup>[15]</sup> In this context, the solubility of pristine PEDOT:PSS films in an aqueous environment is frequently regarded as a limitation, indicating their incompatibility with such conditions. To illustrate the lifetime of PEDOT:PSS in the face of repeated sweeping, Karst et al. demonstrated degradation in photonic response over 290 cycles of sweeping.<sup>[15]</sup> Alternatively, material engineering to enhance the cross-linking of PEDOT:PSS, additive materials could improve the stability in aqueous environment, such as 3-glycidyoxypropyl)trimethoxysilane.<sup>[49]</sup> Nevertheless, it is also imperative to conduct a comprehensive examination of the optical properties as well.

## 2.5. Synaptic Characteristics of ECTP

The innate efficiency and high-speed computing capabilities of parallel and adaptive learning systems have gained significant attention, surpassing the conventional von Neumann architecture.<sup>[50–53]</sup> Optically non-volatile memory devices hold the potential to enable the functionality of photonic neuromorphic systems by allowing precise modulation and sustained maintenance of photonic responses at specific states, guided by hysteresis behavior tied to applied potential and pulsed flux.<sup>[14,15,54]</sup> To achieve a neuromorphic reaction similar to biological systems, two critical aspects come into play: controllability and memorability (Figure 5a). In this context, the ECTP device exhibits a broad range of resistance-voltage (RV) hysteresis, enabling precise control of multiple memory states. Furthermore, its non-volatile property ensures effective retention of optical signals. Much like biological synapses and neurons, the optical state of ECTP is controlled by the counterion corresponding to the applied voltage (Figure 5b, left). The modulation strength is determined by the prior optical state (Figure 5b, right), analogous to how the strength of neural pathways (synaptic weight) between

adjacent neurons in biological systems is influenced by neurotransmitter release and the previous information state, enabling phenomena such as LTP and LTD.

To demonstrate the electrically controlled synaptic weight change (i.e., reflectance change) of the ECTP, we investigated the relationship between synaptic behavior and the number of electrical pulses. Electrical inputs with a pulse width of 50 ms are applied to achieve four stable synaptic weights. Initially, the relative reflectance started below 60%. Subsequently, pulses with a voltage of  $-1$  V (50 ms) were applied, resulting in four distinct states of reflectance with potentiation properties, as depicted in Figure 5c. To achieve depression of the optical signal, pulses with a voltage of  $+1$  V (50 ms) were administered, resulting in a gradual decrease in intensity (Figure 5d). From the measurement, we confirmed the optical state of ECTP is effectively controlled under the pulse of 1 V and showed multiple states of reflectance. Figure 5e represents the optical LTP and LTD behavior observed during the application of 100 pulses at  $-1$  V and  $+1$  V with a frequency of 5 Hz. Under the electrical potentiation pulse ( $-1$  V), the reflectance of ECTP is increased from 43% to 73%. On the contrary, the reflectance decreases from the highest to 42% with an electrical depression pulse ( $+1$  V). The change of reflectance of ECTP corresponds to the applied pulse for potentiation or depression and is distinguishable. The reflectance variation of ECTP approaches saturation at a pulse number of 50, and even after prolonged measurement involving over 100 pulses, it continues to exhibit significant and persistent reflectance variation. Thus, the type and number of applied electrical pulses determine the wide range of optical state of ECTP. We believe that these characteristics of the PEDOT:PSS-based photonic structure hold significant potential for advancing the development of optical neuromorphic systems in the NIR photonic computing/communicating application.

## 3. Conclusion

In summary, this work demonstrated a highly efficient PEDOT:PSS-based optical switch in the NIR range, achieving the highest reported modulation depth to date. The efficient light absorption is achieved by maximizing the light-matter interaction through Tamm plasmon, leading to strong light confinement at the DBR/PEDOT:PSS interface. Despite having intrinsically weak metallic properties ( $\epsilon_r > 0$ ) at  $\omega > \omega_p$ , Tamm plasmon efficiently matches the conjugate impedance, resulting in strong light absorption. The experimental results demonstrate nearly complete absorption in the ECTP state and full reflection in the dielectric state across the NIR range.

Remarkably, even under sub-1-volt operation, which is within the CMOS-compatible voltage range ( $<3.3$  V), the theoretical modulation depth exhibits 99% across the NIR range ( $\lambda_{\text{res}} = 800\text{--}2500$  nm), while the experimental result shows 88% and 80% at  $\lambda_{\text{res}} = 1500$  and 970 nm, respectively. Additionally, applying cyclic voltage induces a hysteresis loop with memory characteristics at the target wavelength ( $\lambda_{\text{res}} = 1500$  nm). Exploiting this property, we successfully demonstrate a programmable ECTP array capable of electrically encoding pre-programmed information, effectively written with a 2-bit level memory state, and successfully read out as ASCII code. ECTP's experimental scalability facilitates production with a 4-inch wafer scale. The controllability and

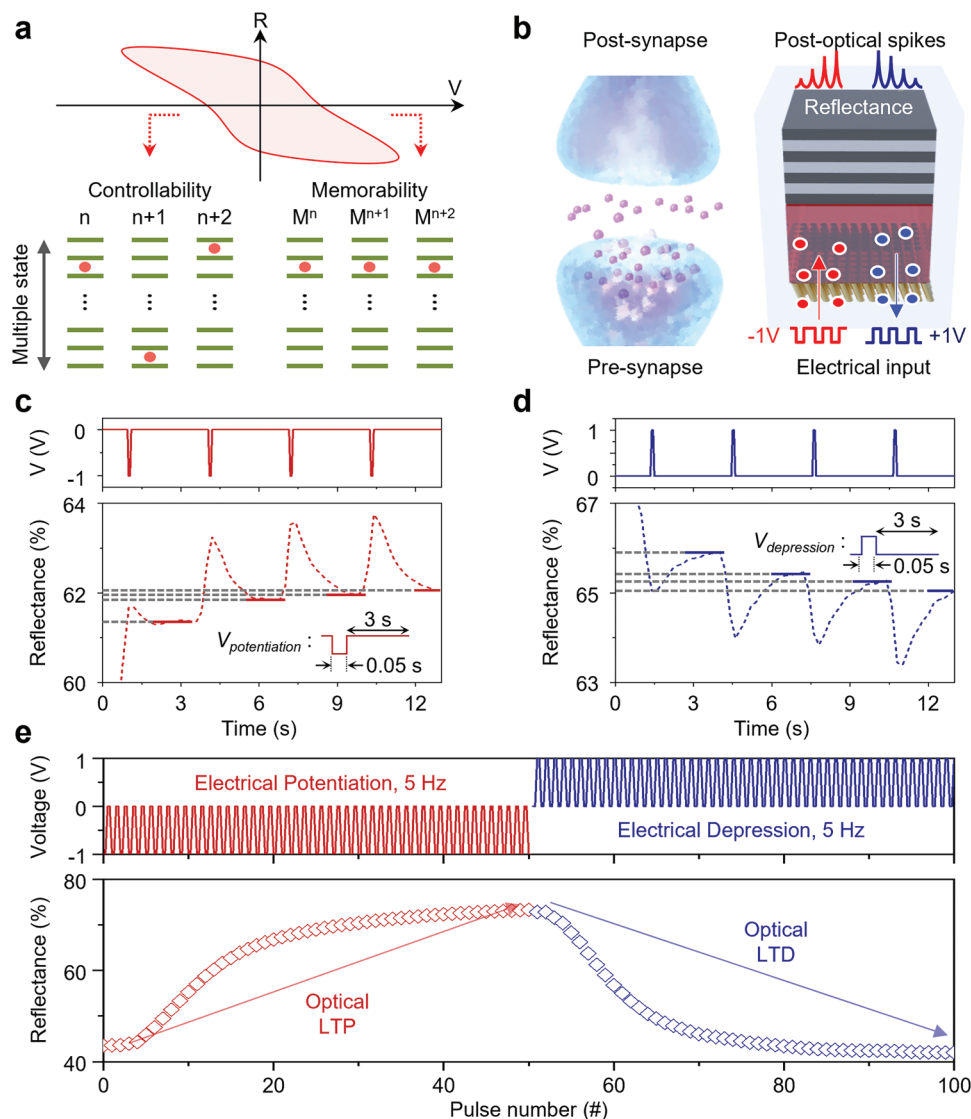


**Figure 5.** PEDOT:PSS-based neuromorphic behavior. a) Controllability and memorability of ECTP induced from the RV hysteresis loop. b) Schematic illustration of ECTP unit cell mimicking the pre-/post-synaptic terminal. Reflectance variation representing c) optical potentiation and d) depression. Voltage of each electrical signal ( $V_{\text{potentiation}}$ ,  $V_{\text{depression}}$ ) is applied for 0.05 s of triggered pulse and 3 s of relaxation. e) Long-term potentiation (LTP) and depression characteristics (LTD) of ECTP under the electrical pre-synaptic terminal of 5 Hz.

memorability of ECTP are also leveraged in exploring its potential as a photonic neuromorphic application. The current state of the electrochemical doping process of PEDOT:PSS achieves the plasma frequency in the NIR range ( $\approx 1300$  nm) and further investigation for ultrahigh doping levels in metallic polymers can open exciting possibilities for pushing their plasma frequency into the visible wavelength range. Based on the approach, we anticipate the ECTP platform to find expanded utility in multi-band operable optical memory and spatial light modulators, maintaining a high on/off ratio with low voltage operation.

The suggested ECTPs and their future engineering directions exhibit remarkable applicability; however, certain issues must be addressed for realistic applications. One notable concern is the slow switching speed compared to immediately responsive active materials like phase change/transition materials (e.g., GST

and  $\text{VO}_2$ )<sup>[55,56]</sup> or electron density tuning materials (e.g., ITO and graphene).<sup>[10,32]</sup> This characteristic may limit the practical application as a switching function, particularly in components requiring fast tuning, such as components in photonic circuits. On the positive side, substantial advantages include freely selectable scalability from the tens of nanometers scale to wafer scale and low operating voltage, overcoming limitations seen in various other tuning materials. In this context, we suggest considering perspectives related to these characteristics, guiding the selection of the active material and photonic structure by considering the target application (Table S2, Supporting Information).

For example, leveraging ECTP, which enables close to 100% intensity control, in conjunction with stacked phase-modulating nanophotonics, could yield a complex spatial light modulator.<sup>[57]</sup> This approach, when viewed from a downsizing perspective,

holds the potential to address crosstalk and integration issues inherent in traditional spatial light modulators, providing a broader optical field of view. Additionally, thanks to the intrinsic CMOS-compatible property of PEDOT:PSS, integration into electronics becomes feasible, contributing significantly to diverse fields such as light detection and ranging (LiDAR) and the development of immersive metaverse platforms. Anticipated expansions encompass applications in holography, augmented reality (AR), and extended reality (XR) devices. In these applications, our proposed demonstration aims to enhance the functionality of futuristic electro-optic devices. For instance, the demonstrated multi-state memorable property of a spatial light modulator could capture preset configurations with diverse states. Additionally, the synaptic behavior, with the property of LTP and LTD, holds the potential for expanding its application into neuromorphic-function integrated photoresponsive applications, that is, in photonic computing.<sup>[58,59]</sup> Meanwhile, addressing the inherent issues of PEDOT:PSS involves aiming for fast modulation times, stability, and uniformity through material engineering. This includes enhancing the ion-diffusion rate, preventing volume expansion, and modifying the deposition method.<sup>[45,46,48]</sup> Another avenue to explore is considering alternative materials, in this context, which could expand the applicability of ECTP into stable function. Materials exhibiting rapid response times and controllable plasma frequencies, such as heavily doped ZnO or doping-controlled conducting oxides, open up intriguing possibilities.<sup>[60,61]</sup> Finally, further investigations on solid electrolytes will accelerate the development of more reliable and safe electrochemical active photonic cells,<sup>[62,63]</sup> bringing us closer to their application in end-to-end commercial product packaging processes.

## 4. Experimental Section

**Fabrication of ECTP:** To realize the designed ECTP, each layer was deposited in three steps. Using plasma-enhanced chemical vapor deposition (PECVD, System 100, Oxford, USA), a DBR was formed with three pairs of insulators ( $\text{SiO}_2/\text{Si}_3\text{N}_4$ ) and the last layer ( $\text{Si}_3\text{N}_4$ ) on a glass substrate. Then, the last layer ( $\text{Si}_3\text{N}_4$ ) was treated with oxygen plasma using a reactive ion etch system (RIE, PLASMA LAB80, Oxford Instruments, UK) to form the hydroxyl groups for the hydrophilic surface before the deposition of PEDOT:PSS active layer. The aqueous dispersion of PEDOT:PSS (PH 1000, Heraeus Clevis, USA) was filtered using a polytetrafluoroethylene syringe filter with a pore size of 0.45  $\mu\text{m}$ . Subsequently, the PEDOT:PSS was spin-coated onto the surface of the last layer ( $\text{Si}_3\text{N}_4$ ) at 650 rpm for 30 s, followed by drying at 120 °C for 15 min to remove the residual solvent. To form a porous Au nanomembrane, the GLAD method was utilized by electron beam evaporation (KVE-E2000, Korea Vacuum Tech Co., Korea) with a customized slanted sample holder at a deposition angle of 70°.<sup>[64,65]</sup> As an adhesion layer, 3 nm of porous Cr layer was deposited. Due to the subwavelength scale of the nanocolumns, the layer exhibited characteristics of an effective medium, effectively avoiding higher-order diffraction.<sup>[66,67]</sup> For the array-patterned ECTP, following the stacking of DBR, each cell's area was defined through a photolithography process. Subsequently, PEDOT:PSS and Cr/Au electrodes were deposited. Finally, the cell and electrodes were defined by a lift-off process. For photolithography, the mask aligner (MJB3 UV400, Karl Suss, Germany), photoresist (AZ 5214, AZ Electronic Materials, Luxembourg), and pre-patterned Cr photo mask were used (Figure S20, Supporting Information).

**Optical Simulation for Design and Analysis of ECTP:** Commercial software (DiffractMOD, RSoft Design Group, Synopsis, USA) based on rigorous coupled-wave analysis was used to calculate the electric field profile and absorption spectra of the ECTP. In the optical simulation, the diffrac-

tion was considered up to second order, and a square grid size of 0.2 nm was set to obtain stable optical efficiency. Materials dispersion and complex refractive indices were also considered. The complex refractive indices of Au,  $\text{SiO}_2$ ,  $\text{Si}_3\text{N}_4$ , ITO, GST,  $\text{VO}_2$ , and PEDOT:PSS were obtained from the literature.<sup>[15,68–75]</sup> To calculate the effective refractive index of the porous Au membrane, volume averaging theory was used, and it was calculated using MATLAB (Mathworks, Inc.).

**Electrochemical Setup and Measurement:** The electrochemical setup was composed of a potentiostat (PARSTAT4000A, AMETEK, USA), reference electrode (silver/silver-chloride, Ag/AgCl), counter electrode (Pt mesh), and electrolyte (0.1 mol L<sup>-1</sup> TBAPF<sub>6</sub> in acetonitrile). The electrolyte was prepared by dissolving the tetrabutylammonium hexafluorophosphate (TBAPF-6, Sigma Aldrich) in acetonitrile (anhydrous 99.8%, Sigma Aldrich).

**Optical Characterization and Measurement:** The absorption spectra and optical hysteresis properties of the ECTP were analyzed employing a UV-VIS-NIR spectrometer (LAMBDA 950, Perkin Elmer, USA). For SWIR imaging, a SWIR camera (ABA-003VIR, Aval, Japan) was mounted with an objective lens (NV5014SWIR, AZURE, China). SWIR imaging of the ECTP was conducted at a normal angle of incidence while being illuminated by a tungsten-halogen lamp as the light source, with the assistance of a 12.5 mm diameter bandpass filter (FBH051550-40, 1483–1617 nm, Thorlabs, USA). The measured optical power density illuminating the ECTPs was recorded at 15.8 W m<sup>-2</sup>, a level considered safe and unlikely to cause damage to the PEDOT:PSS through photothermal effects (Note 2 and Figure S6, Supporting Information). Additionally, electrochemical in situ doping and dedoping procedures were performed during the measurement process using a potentiostat (PalmSens4, PalmSens, Netherlands), as illustrated in Figure S21, Supporting Information.

## Supporting Information

Supporting Information is available from the Wiley Online Library or from the author.

## Acknowledgements

This work was supported by the GIST Research Institute (GRI) RISE, GIST-MIT Research Collaboration, Startup Acceleration Centre, and AI-based GIST Research Scientist Project through a grant funded by the GIST. This work was also supported by the National Research Foundation of Korea (NRF) funded by the Ministry of Science and ICT (NRF-2023R1A2C3004531, NRF-2021M3H4A1A04086357, NRF-2022M3C1A3081312), the regional innovation mega project program through the Korea Innovation Foundation funded by the Ministry of Science and ICT (2023-DD-UP-0015), and KRIT—grant funded by the Defense Acquisition Program Administration (DAPA) (21-406-B00-005).

## Conflict of Interest

The authors declare no conflict of interest.

## Author Contributions

J.H.K. and D.H.S. contributed equally to this work. J.H.K., D.H.S., H.-H.J., and Y.M.S. conceived the idea and designed the whole experiment. J.H.K. and D.H.S. developed the process and fabricated the samples. J.H.K., D.H.S., S.K., and Y.M.S. conceived the experiments and analyzed the data. J.H.K., S.K., and Y.M.S. mainly wrote the manuscript. D.H.S., H.-H.J., and Y.M.S. edited the manuscript. All the authors confirmed the final manuscript. Y.M.S. guided the entire project.

## Data Availability Statement

The data that support the findings of this study are available from the corresponding author upon reasonable request.

## Keywords

electrically switchable, photonics crystal, poly (3,4-ethylene-dioxythiophene):polystyrene sulfonate, reconfigurable photonics, Tamm plasmon

Received: October 11, 2023

Revised: November 26, 2023

Published online:

- [1] D. Marpaung, J. Yao, J. Capmany, *Nat. Photonics* **2019**, *13*, 80.
- [2] L. Liu, L. Kang, T. S. Mayer, D. H. Werner, *Nat. Commun.* **2016**, *7*, 13236.
- [3] M. Wuttig, H. Bhaskaran, T. Taubner, *Nat. Photonics* **2017**, *11*, 465.
- [4] A. M. Shaltout, V. M. Shalae, M. L. Brongersma, *Science* **2019**, *364*, eaat3100.
- [5] I.-C. Benea-Chelmus, M. L. Meretska, D. L. Elder, M. Tamagnone, L. R. Dalton, F. Capasso, *Nat. Commun.* **2021**, *12*, 5928.
- [6] I.-C. Benea-Chelmus, S. Mason, M. L. Meretska, D. L. Elder, D. Kazakov, A. Shams-Ansari, L. R. Dalton, F. Capasso, *Nat. Commun.* **2022**, *13*, 3170.
- [7] N. Jeon, J. Noh, C. Jung, J. Rho, *New J. Phys.* **2022**, *24*, 075001.
- [8] G. Kafaie Shirmanesh, R. Sokhoyan, R. A. Pala, H. A. Atwater, *Nano Lett.* **2018**, *18*, 2957.
- [9] J. Park, J.-H. Kang, S. J. Kim, X. Liu, M. L. Brongersma, *Nano Lett.* **2017**, *17*, 407.
- [10] A. Forouzmmand, H. Mosallaei, *ACS Photonics* **2019**, *6*, 2860.
- [11] Y. Zhang, C. Fowler, J. Liang, B. Azhar, M. Y. Shalaginov, S. Deckoff-Jones, S. An, J. B. Chou, C. M. Roberts, V. Liberman, M. Kang, C. Ríos, K. A. Richardson, C. Rivero-Baleine, T. Gu, H. Zhang, J. Hu, *Nat. Nanotechnol.* **2021**, *16*, 661.
- [12] Y. Zhang, J. B. Chou, J. Li, H. Li, Q. Du, A. Yadav, S. Zhou, M. Y. Shalaginov, Z. Fang, H. Zhong, C. Roberts, P. Robinson, B. Bohlin, C. Ríos, H. Lin, M. Kang, T. Gu, J. Warner, V. Liberman, K. Richardson, J. Hu, *Nat. Commun.* **2019**, *10*, 4279.
- [13] J. Yang, S. Gurung, S. Bej, P. Ni, H. W. Howard Lee, *Rep. Prog. Phys.* **2022**, *85*, 036101.
- [14] N. Youngblood, C. A. Ríos Ocampo, W. H. Pernice, H. Bhaskaran, *Nat. Photonics* **2023**, *17*, 561.
- [15] J. Karst, M. Floess, M. Ubl, C. Dingler, C. Malacrida, T. Steinle, S. Ludwigs, M. Hentschel, H. Giessen, *Science* **2021**, *374*, 612.
- [16] C. Wang, M. Zhang, X. Chen, M. Bertrand, A. Shams-Ansari, S. Chandrasekhar, P. Winzer, M. Loncar, *Nature* **2018**, *562*, 101.
- [17] J. Zheng, Z. Fang, C. Wu, S. Zhu, P. Xu, J. K. Doyle, S. Deshmukh, E. Pop, S. Dunham, M. Li, A. Majumdar, *Adv. Mater.* **2020**, *32*, 2001218.
- [18] Z. Fang, R. Chen, J. Zheng, A. I. Khan, K. M. Neilson, S. J. Geiger, D. M. Callahan, M. G. Moebius, A. Saxena, M. E. Chen, C. Ríos, J. Hu, E. Pop, A. Majumdar, *Nat. Nanotechnol.* **2022**, *17*, 842.
- [19] H. Eoh, H. S. Kang, M. J. Kim, M. Koo, T. H. Park, Y. Kim, H. Lim, D. Y. Ryu, E. Kim, J. Huh, Y. Kang, C. Park, *Adv. Funct. Mater.* **2019**, *29*, 1904055.
- [20] Z. Zhu, P. G. Evans, R. F. Haglund, J. G. Valentine, *Nano Lett.* **2017**, *17*, 4881.
- [21] Y. Kim, P. C. Wu, R. Sokhoyan, K. Mauser, R. Glauddell, G. Kafaie Shirmanesh, H. A. Atwater, *Nano Lett.* **2019**, *19*, 3961.
- [22] L. Ye, K. Sui, Y. Liu, M. Zhang, Q. H. Liu, *Opt. Express* **2018**, *26*, 15935.
- [23] X. Tian, J. Xu, K. Xu, X. Ma, X. Duan, P. Yang, P. Ding, Z.-Y. Li, *Europhys. Lett.* **2020**, *128*, 67001.
- [24] A. Tittl, A.-K. U. Michel, M. Schäferling, X. Yin, B. Gholipour, L. Cui, M. Wuttig, T. Taubner, F. Neubrech, H. Giessen, *Adv. Mater.* **2015**, *27*, 4597.
- [25] J. Karst, Y. Lee, M. Floess, M. Ubl, S. Ludwigs, M. Hentschel, H. Giessen, *Nat. Commun.* **2022**, *13*, 7183.
- [26] S. H. Kim, J. H. Ko, Y. J. Yoo, M. S. Kim, G. J. Lee, S. Ishii, Y. M. Song, *Adv. Opt. Mater.* **2022**, *10*, 2102388.
- [27] M. He, J. R. Nolen, J. Nordlander, A. Cleri, N. S. McIlwaine, Y. Tang, G. Lu, T. G. Folland, B. A. Landman, J.-P. Maria, J. D. Caldwell, *Nat. Mater.* **2021**, *20*, 1663.
- [28] H. Zhao, R. Zhang, H. T. Chorsi, W. A. Britton, Y. Chen, P. P. Iyer, J. A. Schuller, L. D. Negro, J. Klamkin, *Nanophotonics* **2019**, *8*, 1803.
- [29] Y. Yao, R. Shankar, M. A. Kats, Y. Song, J. Kong, M. Loncar, F. Capasso, *Nano Lett.* **2014**, *14*, 6526.
- [30] B. Zeng, Z. Huang, A. Singh, Y. Yao, A. K. Azad, A. D. Mohite, A. J. Taylor, D. R. Smith, H.-T. Chen, *Light: Sci. Appl.* **2018**, *7*, 51.
- [31] M. Amin, M. Farhat, H. Bagci, *Sci. Rep.* **2013**, *3*, 2105.
- [32] Z. Fei, A. S. Rodin, G. O. Andreev, W. Bao, A. S. McLeod, M. Wagner, L. M. Zhang, Z. Zhao, M. Thiemens, G. Dominguez, M. M. Fogler, A. H. C. Neto, C. N. Lau, F. Keilmann, D. N. Basov, *Nature* **2012**, *487*, 82.
- [33] Z. Sámson, K. MacDonald, F. De Angelis, B. Gholipour, K. Knight, C. Huang, E. Di Fabrizio, D. Hewak, N. Zheludev, *Appl. Phys. Lett.* **2010**, *96*, 143105.
- [34] S. Abdollahramezani, O. Hemmatyar, M. Taghinejad, H. Taghinejad, A. Krasnok, A. A. Eftekhar, C. Teichrib, S. Deshmukh, M. A. El-Sayed, E. Pop, M. Wuttig, A. Alù, W. Cai, A. Adibi, *Nat. Commun.* **2022**, *13*, 1696.
- [35] T. Cao, R. E. Simpson, M. J. Cryan, *J. Opt. Soc. Am. B* **2013**, *30*, 439.
- [36] L. T. Chew, W. Dong, L. Liu, X. Zhou, J. Behera, H. Liu, K. V. Sreekanth, L. Mao, T. Cao, J. Yang, presented at Active Photonic Platforms IX, San Diego, California, United States, August **2017**.
- [37] R. Zhang, Y. Luo, J. Xu, H. Wang, H. Han, D. Hu, Q. Zhu, Y. Zhang, *Opt. Express* **2021**, *29*, 42989.
- [38] J. H. Ko, Y. J. Yoo, Y. Lee, H.-H. Jeong, Y. M. Song, *iScience* **2022**, *25*, 104727.
- [39] A. Forouzmmand, M. M. Salary, S. Inampudi, H. Mosallaei, *Adv. Opt. Mater.* **2018**, *6*, 1701275.
- [40] M. C. Sherrott, P. W. C. Hon, K. T. Fountaine, J. C. Garcia, S. M. Ponti, V. W. Brar, L. A. Sweatlock, H. A. Atwater, *Nano Lett.* **2017**, *17*, 3027.
- [41] Z.-Y. Yang, S. Ishii, T. Yokoyama, T. D. Dao, M.-G. Sun, P. S. Pankin, I. V. Timofeev, T. Nagao, K.-P. Chen, *ACS Photonics* **2017**, *4*, 2212.
- [42] Y. Tsurimaki, J. K. Tong, V. N. Boriskin, A. Semenov, M. I. Ayzatsky, Y. P. Machehkin, G. Chen, S. V. Boriskina, *ACS Photonics* **2018**, *5*, 929.
- [43] M. Backholm, M. Foss, K. Nordlund, *Appl. Surf. Sci.* **2013**, *268*, 270.
- [44] R. El Beainou, A. Chargui, P. Pedrosa, A. Mosset, S. Euphrasie, P. Vairac, N. Martin, *Appl. Surf. Sci.* **2019**, *475*, 606.
- [45] C. Cea, G. D. Spyropoulos, P. Jastrzebska-Perfect, J. J. Ferrero, J. N. Gelinas, D. Khodagholy, *Nat. Mater.* **2020**, *19*, 679.
- [46] Y. Lee, J. Karst, M. Ubl, M. Hentschel, H. Giessen, *Nanophotonics* **2023**, *12*, 2865.
- [47] M. S. Park, Y. Lee, J. K. Kim, *Chem. Mater.* **2005**, *17*, 3944.
- [48] I. Muguet, A. Maziz, F. Mathieu, L. Mazenq, G. Larrieu, *Adv. Mater.* **2023**, *35*, 2302472.
- [49] A. Håkansson, S. Han, S. Wang, J. Lu, S. Braun, M. Fahlman, M. Berggren, X. Crispin, S. Fabiano, *J. Polym. Sci., Part B: Polym. Phys.* **2017**, *55*, 814.
- [50] P. Lin, C. Li, Z. Wang, Y. Li, H. Jiang, W. Song, M. Rao, Y. Zhuo, N. K. Upadhyay, M. Barnell, Q. Wu, J. J. Yang, Q. Xia, *Nat. Electron.* **2020**, *3*, 225.
- [51] Z. Cheng, C. Ríos, W. H. P. Pernice, C. D. Wright, H. Bhaskaran, H. Bhaskaran, *Sci. Adv.* **2017**, *3*, e1700160.
- [52] M.-K. Song, J.-H. Kang, X. Zhang, W. Ji, A. Ascoli, I. Messaris, A. S. Demirkol, B. Dong, S. Aggarwal, W. Wan, S.-M. Hong, S. G. Cardwell, I. Boybat, J.-S. Seo, J.-S. Lee, M. Lanza, H. Yeon, M. Onen, J. Li, B. Yildiz, J. A. Del Alamo, S. Kim, S. Choi, G. Milano, C. Ricciardi, L. Aliff, Y. Chai, Z. Wang, H. Bhaskaran, M. C. Hersam, et al., *ACS Nano* **2023**, *17*, 11994.

- [53] F. Zhou, Z. Zhou, J. Chen, T. H. Choy, J. Wang, N. Zhang, Z. Lin, S. Yu, J. Kang, H.-S. P. Wong, Y. Chai, *Nat. Nanotechnol.* **2019**, *14*, 776.
- [54] W. Liang, G. Li, Q. Zhou, Z. Zhang, S. Zhang, T. Ning, P. Zhang, Y. Deng, C. Zhang, C. Ge, *Appl. Phys. Lett.* **2023**, *122*, 071702.
- [55] T. Gu, H. J. Kim, C. Rivero-Baleine, J. Hu, *Nat. Photonics* **2022**, *17*, 48.
- [56] Y. Zhang, C. Fowler, J. Liang, B. Azhar, M. Y. Shalaginov, S. Deckoff-Jones, S. An, J. B. Chou, C. M. Roberts, V. Liberman, M. Kang, C. Ríos, K. A. Richardson, C. Rivero-Baleine, T. Gu, H. Zhang, J. Hu, *Nat. Nanotechnol.* **2021**, *16*, 661.
- [57] T. Chang, J. Jung, S.-H. Nam, H. Kim, J. U. Kim, N. Kim, S. Jeon, M. Heo, J. Shin, *Adv. Mater.* **2022**, *34*, 2204085.
- [58] S. H. Kim, G. W. Baek, J. Yoon, S. Seo, J. Park, D. Hahm, J. H. Chang, D. Seong, H. Seo, S. Oh, K. Kim, H. Jung, Y. Oh, H. W. Baac, B. Alimkhanuly, W. K. Bae, S. Lee, M. Lee, J. Kwak, J.-H. Park, D. Son, *Adv. Mater.* **2021**, *33*, 2104690.
- [59] B. J. Shastri, A. N. Tait, T. Ferreira De Lima, W. H. P. Pernice, H. Bhaskaran, C. D. Wright, P. R. Prucnal, *Nat. Photonics* **2021**, *15*, 102.
- [60] A. Koch, H. Mei, J. Rensberg, M. Hafermann, J. Salman, C. Wan, R. Wambold, D. Blaschke, H. Schmidt, J. Salfeld, S. Geburt, M. A. Kats, C. Ronning, *Adv. Photonics Res.* **2023**, *4*, 2200181.
- [61] H. Mei, A. Koch, C. Wan, J. Rensberg, Z. Zhang, J. Salman, M. Hafermann, M. Schaal, Y. Xiao, R. Wambold, S. Ramanathan, C. Ronning, M. A. Kats, *Nanophotonics* **2022**, *11*, 3923.
- [62] Y. Van De Burgt, E. Lubberman, E. J. Fuller, S. T. Keene, G. C. Faria, S. Agarwal, M. J. Marinella, A. Alec Talin, A. Salleo, *Nat. Mater.* **2017**, *16*, 414.
- [63] Z. Shao, A. Huang, C. Ming, J. Bell, P. Yu, Y.-Y. Sun, L. Jin, L. Ma, H. Luo, P. Jin, X. Cao, *Nat. Electron.* **2022**, *5*, 45.
- [64] J. H. Ko, Y. J. Yoo, Y. J. Kim, S.-S. Lee, Y. M. Song, *Adv. Funct. Mater.* **2020**, *30*, 1908592.
- [65] Y. J. Yoo, W.-G. Kim, J. H. Ko, Y. J. Kim, Y. Lee, S. G. Stanciu, J.-M. Lee, S. Kim, J.-W. Oh, Y. M. Song, *Adv. Sci.* **2020**, *7*, 2000978.
- [66] Y. J. Yoo, J. H. Ko, G. J. Lee, J. Kang, M. S. Kim, S. G. Stanciu, H.-H. Jeong, D.-H. Kim, Y. M. Song, *Adv. Mater.* **2022**, *34*, 2110003.
- [67] J. H. Ko, J.-H. Park, Y. J. Yoo, S. Chang, J. Kang, A. Wu, F. Yang, S. Kim, H.-G. Jeon, Y. M. Song, *Adv. Sci.* **2023**, *10*, 2304310.
- [68] K. Luke, Y. Okawachi, M. R. E. Lamont, A. L. Gaeta, M. Lipson, *Opt. Lett.* **2015**, *40*, 4823.
- [69] L. Gao, F. Lemarchand, M. Lequime, *Opt. Express* **2012**, *20*, 15734.
- [70] J. Zheng, A. Khanolkar, P. Xu, S. Colburn, S. Deshmukh, J. Myers, J. Frantz, E. Pop, J. Hendrickson, J. Doyle, N. Boechler, A. Majumdar, J. Doyle, *Opt. Mater. Express* **2018**, *8*, 1551.
- [71] P. B. Johnson, R. W. Christy, *Phys. Rev. B* **1972**, *6*, 4370.
- [72] I. Derkaoui, M. Khenfouch, M. Benkhali, A. Rezzouk, *J. Phys.: Conf. Ser.* **2019**, *1292*, 012010.
- [73] S. Xian, L. Nie, J. Qin, T. Kang, C. Li, J. Xie, L. Deng, L. Bi, *Opt. Express* **2019**, *27*, 28618.
- [74] J. Faneca, S. Garcia-Cuevas Carrillo, E. Gemo, C. R. De Galarreta, T. Domínguez Bucio, F. Y. Gardes, H. Bhaskaran, W. H. P. Pernice, C. D. Wright, A. Baldycheva, *Opt. Mater. Express* **2020**, *10*, 1778.
- [75] C. Dingler, R. Walter, B. Gompf, S. Ludwigs, *Macromolecules* **2022**, *55*, 1600.